



HAL
open science

Interglacial instability of North Atlantic Deep Water ventilation

Eirik Vinje Galaasen, Ulysses Ninnemann, Augustin Kessler, Nil Irvani, Yair Rosenthal, Jerry Tjiputra, Nathaëlle Bouttes, Didier M. Roche, Helga (kikki) F. Kleiven, David Hodell

► **To cite this version:**

Eirik Vinje Galaasen, Ulysses Ninnemann, Augustin Kessler, Nil Irvani, Yair Rosenthal, et al.. Interglacial instability of North Atlantic Deep Water ventilation. *Science*, 2020, 367 (6485), pp.1485-1489. 10.1126/science.aay6381 . hal-02968727

HAL Id: hal-02968727

<https://hal.science/hal-02968727>

Submitted on 7 Dec 2020

HAL is a multi-disciplinary open access archive for the deposit and dissemination of scientific research documents, whether they are published or not. The documents may come from teaching and research institutions in France or abroad, or from public or private research centers.

L'archive ouverte pluridisciplinaire **HAL**, est destinée au dépôt et à la diffusion de documents scientifiques de niveau recherche, publiés ou non, émanant des établissements d'enseignement et de recherche français ou étrangers, des laboratoires publics ou privés.

30 **One Sentence Summary:** Large and frequent changes in ocean ventilation during recent warm
31 periods question its modern stability.

32 **Main Text:** Atlantic meridional overturning circulation (AMOC) and North Atlantic Deep
33 Water (NADW) ventilation represents a low probability, high impact tipping point (*1*) in the
34 climate system with implications for the distribution and sequestration of anthropogenic CO₂
35 and heat, and for Atlantic-wide patterns of climate and sea level (*2-4*). While the consequences
36 of any changes are clearly severe, the probability for instabilities in the rate or pathways of
37 NADW ventilation remains highly uncertain. Simple and complex models both suggest large
38 changes are possible, but also that a strong overturning like that found in the modern ocean
39 may be more difficult to disrupt than an overall weaker circulation (*4-6*). Likewise, most
40 models simulate moderate to no reduction in AMOC in response to future source region
41 buoyancy increases (*1*) but may be biased towards stability (*7*) and struggle to reproduce the
42 rich spectrum of variability revealed by a decade of observations (*8, 9*). Testing these physical
43 and conceptual models, and more generally the stability of NADW ventilation in warm
44 climates, requires empirical constraints from beyond the current state of circulation.

45 Given a background climate similar to today, the modern mode of deep Atlantic
46 ventilation with strong NADW influence (Fig. 1) appears stable on long multi-millennial
47 timescales. Proxy reconstructions indicate that modern NADW ventilation pathways persisted
48 with little multi-millennial variability in recent interglacial periods (*10-14*). By contrast,
49 pronounced AMOC variability has occurred on timescales of a decade or less in observations
50 (*8, 9*) suggesting strong mean overturning is comprised of significant variance. However, little
51 is known about NADW variability on the intermediary timescales, leaving the variability
52 within a long-term ‘vigorous’ mean ventilation state poorly defined. There are few proxy

53 reconstructions depicting higher-frequency variability and those available are largely confined
54 to the last two interglacials, the Holocene and Marine Isotope Stage (MIS) 5e. During these
55 periods, the largest changes in deep Atlantic ventilation involving reductions of NADW
56 influence occurred on relatively short centennial timescales and were focused around intervals
57 with wasting of continental ice sheet remnants from the preceding glaciation (10, 12, 15). This
58 includes the century-long NADW reduction at 8.2 thousand years (ky) before present (B.P.)
59 following the freshwater outburst flood from glacial Lake Agassiz (12). Absence of similarly
60 large changes in the last ~eight ky of the Holocene (e.g., 12) has supported the notion of
61 vigorous and stable ventilation as generally representative of interglacial boundary conditions.

62 Beyond the last two interglacials, little is known about centennial-scale variability in
63 NADW, despite its relevance for delimiting the natural variability of ocean ventilation and the
64 frequency of large NADW reductions under different background climates. The most recent
65 interglacials MIS 5e, 7e, 9e, and 11c are particularly relevant, as these periods had similar
66 climate boundary conditions to the current MIS 1 in addition to episodes of high-latitude
67 warming, Greenland Ice Sheet (GrIS) retreat, and sea level rise relative to the modern (16-18).
68 This offers an opportunity to test the robustness of NADW ventilation under source region
69 conditions similar to those projected for the future (1). Here we reconstruct northwest Atlantic
70 bottom water $\delta^{13}\text{C}$ to trace NADW influence (Fig. 1) over MIS 7e, 9e, and 11c and provide a
71 detailed perspective on NADW ventilation instability during recent interglacials.

72 Our epibenthic foraminifera *Cibicidoides wuellerstorfi* (sensu stricto) $\delta^{13}\text{C}$ record (19)
73 from International Ocean Drilling Program (IODP) Site U1305 (57°29'N, 48°32'W; 3459 m
74 water depth) at the Eirik Drift is situated to monitor lower NADW entering the deep Atlantic
75 (Fig. 1). Due to the potential for uncertainty in $\delta^{13}\text{C}$ reconstructions (e.g., 20), we only consider

76 changes in the running mean of three samples (averaging five data points; see (19)) and signals
77 outside the standard error of data within this window to reflect bottom water $\delta^{13}\text{C}$ variability,
78 which, given negligible influence from organic carbon fluxes (21), provides a proxy for past
79 changes in the ventilation and distribution of water masses (e.g., 20, 22). The Eirik Drift
80 bottom water $\delta^{13}\text{C}$ record indicates large changes in deep Atlantic carbon chemistry during the
81 interglacial $\delta^{18}\text{O}$ plateaus of MIS 7e, 9e, and 11c (Fig. 2). Each interglacial contained abrupt
82 changes in bottom water $\delta^{13}\text{C}$ as large ($\leq 1.0\text{‰}$) as those of the bordering glacial terminations
83 and inceptions (Fig. 2), and similar to those occurring after freshwater outburst floods such as
84 the ~ 8.2 ky B.P. event (12) and during MIS 5e (10). Absolute values range from near modern
85 NADW levels ($\geq 0.8\text{‰}$; Fig. 1) to those typical of the glacial deep Atlantic (13, 14, 23, 24).
86 While similar in magnitude, the frequency, timing, and duration of these changes differ among
87 individual interglacial periods. Low bottom water $\delta^{13}\text{C}$ values persist for a millennium or more
88 during late MIS 7e ($\sim 233.5\text{--}243.5$ ky; on our age model, 19) and mid- to late MIS 9e ($\sim 323.0\text{--}$
89 326.0 ky), whereas large ($\sim 0.5\text{‰}$) multi-centennial variability punctuated MIS 11c
90 superimposed on multi-millennial trends.

91 Low bottom water $\delta^{13}\text{C}$ values at Site U1305 likely reflect reduced NADW influence
92 and changes in deep Atlantic ventilation patterns. Reduced (high- $\delta^{13}\text{C}$) NADW influence and
93 incursions of (low- $\delta^{13}\text{C}$) Southern source water (SSW) explain many features of the observed
94 variability, including the: 1) spatial consistency of intermittently low $\delta^{13}\text{C}$ observed at different
95 deep sites (Site U1304 and U1305; Fig. 3); 2) abruptness of the $\delta^{13}\text{C}$ changes as the NADW-
96 SSW water mass boundary shifted across the core sites; 3) shift of Site U1305 $\delta^{13}\text{C}$ towards the
97 millennially averaged values found near the northern or the southern source regions (Fig. 3);

98 and 4) association of high (low) *C. wuellerstorfi* $\delta^{13}\text{C}$ with high (low) *C. wuellerstorfi* B/Ca in
99 selected Eirik Drift samples (Fig. S6) (19).

100 We further use a transient interglacial (115-125 ky) simulation (19) with the isotope-
101 enabled intermediate complexity iLOVECLIM Earth system model (25) to assess potential
102 links between variability in deep Atlantic $\delta^{13}\text{C}$, NADW distribution, and AMOC. Simulated
103 centennial-scale episodes of NADW shoaling and SSW expansion produce $\delta^{13}\text{C}$ reductions in
104 the deep Atlantic that strongly match the magnitude, rate and duration of the variability
105 observed in our (Fig. 4) and other reconstructions (e.g., 10, 12-14) consistent with the inference
106 that the $\delta^{13}\text{C}$ variability reflect changes in NADW distribution. These large deep Atlantic $\delta^{13}\text{C}$
107 changes, which are similar in magnitude to glacial millennial-scale changes (e.g., 23, 24), were
108 achieved without a total collapse of but with a significant (~16 to ~8 Sv) decrease in AMOC
109 strength and accompanied by cooling in the subpolar North Atlantic (Fig. 4).

110 Our results call for reconsideration of the long-held notion of warm-climate stability in
111 deep Atlantic carbon chemistry and ventilation. This view of stability likely remains true for
112 the (multi-)millennial mean state, as previously depicted by lower-resolution records lacking
113 the fidelity to resolve the shorter timescale that is characteristic of NADW reductions (Fig. 3).
114 High-resolution records are naturally biased towards the youngest strata and the current
115 interglacial, the Holocene. Yet, when contextualized against the late Pleistocene interglacials,
116 the Holocene stands out as having had the most stable lower NADW ventilation of the last half
117 million years (Fig. 3), which was only strongly curtailed at ~8.2 ky B.P. (12). Bottom water
118 $\delta^{13}\text{C}$ and NADW reductions similar to that at ~8.2 ky B.P. were prevalent features of prior
119 interglacials, occasionally even lasting millennia (Fig. 3). Ventilation patterns changed
120 repeatedly from one similar to the modern (Fig. 1) to one with reduced NADW and incursions

121 of SSW in the deep North Atlantic (~3.4 km), similar to that illustrated by our model
122 simulation (Fig. 4).

123 The short duration of interglacial NADW reductions may indicate a change in the
124 intrinsic ocean dynamics operating under different background climate states. The interglacial
125 deep Atlantic is clearly better ventilated than the glacial on long equilibrium timescales (11, 13,
126 14, 23, 24). However, the magnitude of ventilation pattern changes that are possible appears
127 similar in (de-)glacial (e.g., 11, 24, 26) and interglacial periods when variability in lower
128 NADW is considered at shorter timescales (Fig. 3). The centennial-scale duration and transient
129 nature of most interglacial NADW reductions (Fig. 3; Fig. 4) suggests the modern ventilation
130 pattern tends to recover quickly when perturbed, and is similar to the AMOC recovery
131 timescale seen in many numerical models forced with buoyancy increases (e.g., 4). With this in
132 mind, the longer-lasting NADW reductions in MIS 7e (~233.5-234.5 ky), 9e (~323-326 ky),
133 and late 11c (~401-408 ky) either required more sustained forcing or suggests that the recovery
134 timescale following perturbations is not fixed. Most interglacial NADW reductions were still
135 short-lived compared to those associated with glacial (Dansgaard-Oeschger) variability (e.g.,
136 24), suggesting either that NADW ventilation behaved differently or the persistence of any
137 forcing changed, depending on the climate state. One possible explanation for this timescale
138 difference is the extensive glacial expansion of high-latitude sea ice, which could promote a
139 baseline increase in SSW ventilation (27) and prolong the duration of northern ventilation
140 anomalies (28). A lack of strong sea ice responses could also explain the potentially muted
141 climate variability in interglacial compared to glacial climates (10, 13, 14, 29), despite the
142 presence of NADW variability. More high-resolution climate records spanning past
143 interglacials are however needed to conclusively evaluate the impacts of warm-climate NADW

144 reductions, and delineate its role relative feedbacks such as sea ice responses in driving
145 interglacial climate variability.

146 Model simulations suggest future warming and freshwater addition from an intensified
147 hydrological cycle and ice sheet melting could all increase source region buoyancy and curtail
148 convective NADW renewal (1, 4). The common occurrence of NADW reductions in past
149 interglacials (Fig. 3) clearly demonstrates the potential for large changes in deep Atlantic
150 ventilation and allows us to explore the triggers for perturbations. NADW reductions during
151 the last two interglacial periods were confined mainly to the early warm interglacial phases,
152 concurrent with high northern hemisphere summer insolation and known freshwater outburst
153 floods accompanying the final retreat of residual glacial ice sheets (Fig. 3) (10, 12, 30, 31).
154 While stratigraphically belonging to interglacial periods, to the extent that these anomalies are
155 related to wasting vestiges of glaciation, they are likely best viewed mechanistically as the final
156 episodes of deglaciation. By contrast, NADW reductions in MIS 7e, 9e, and 11c occurred in
157 the mid and late interglacial phases under low summer insolation (Fig. 3) and after any likely
158 deglacial freshwater influences. This implies that NADW reductions can occur without the
159 excess buoyancy input provided by wasting residual glacial ice sheets, or the influence of large
160 continental ice sheets on atmospheric circulation. Ice sheet activity may still have played a role
161 in regulating the stability of NADW ventilation during some periods. NADW reductions in
162 MIS 7e, 9e, and 11c often coincided with, or were preceded by, input of ice-rafted debris (IRD)
163 at Site U1305 (Fig. 3), indicating supply of icebergs and freshwater proximal to the NADW
164 source region. Furthermore, the prolonged NADW reduction of MIS 9e was associated with
165 elevated southern GrIS sediment discharge and MIS 1 stability with low GrIS activity (32),
166 while particularly strong GrIS retreat in MIS 11c (16, 18) occurred alongside persistent NADW

167 variability (Fig. 3). These observations are consistent with ice sheet activity and freshwater
168 addition intermittently influencing the formation or downstream density of lower NADW.
169 However, variability in NADW ventilation, IRD input, and GrIS discharge also occurred
170 independently of each other (Fig. 3), implicating additional controls on NADW ventilation and
171 supporting models suggesting convective instability is possible with relatively small buoyancy
172 input if delivered to the convection regions (e.g., 6).

173 Our results suggest we should consider rapid and large changes in NADW ventilation
174 not only as a possibility (10, 12, 30) but even as an intrinsic feature of centennial-scale
175 variability in warm climate states. This has implications for constraining the potential for and
176 cause of change in the modern Atlantic. First, it supports concerns that disregarding large
177 variability in simulations may have biased future AMOC projections towards stability (7). The
178 possibility of large natural variability on decadal (8, 9) to centennial timescales (Fig. 3) also
179 complicates attribution of variability in the deep Atlantic, but the characteristics of this
180 variability may be used to differentiate between natural and anthropogenic change in the
181 coming century. While past changes were predominantly multi-centennial, there are also
182 climate and ocean conditions that can drive longer NADW reductions, as evidenced for
183 example by the ~3000 years-long anomaly in mid-MIS 9e (Fig. 3). Specifically what these
184 conditions were remains unclear, but the triggers for NADW instability have clearly operated
185 across the range of recent interglacial climate conditions. Recognizing this requires moving
186 beyond the notion of vigorous and stable deep Atlantic ventilation as representative of warm
187 climate states (e.g., 1, 5, 11), and towards conceptual and numerical models that can account
188 for pronounced variability across various timescales and climate states.

189

190 **References and Notes:**

- 191 1. IPCC, in *Climate Change 2013: The Physical Science Basis. Contribution of Working*
192 *Group I to the Fifth Assessment Report of the Intergovernmental Panel on Climate*
193 *Change*, T. F. Stocker *et al.*, Eds., *Summary for Policymakers* (Cambridge Univ. Press,
194 Cambridge, United Kingdom and New York, NY, USA, 2013).
- 195 2. M. W. Buckley, J. Marshall, Observations, inferences, and mechanisms of the Atlantic
196 Meridional Overturning Circulation: A review. *Reviews of Geophysics* **54**, 5-63 (2016).
- 197 3. C. L. Sabine *et al.*, The oceanic sink for anthropogenic CO₂. *Science* **305**, 367-371
198 (2004).
- 199 4. T. F. Stocker, A. Schmittner, Influence of CO₂ emission rates on the stability of the
200 thermohaline circulation. *Nature* **388**, 862-865 (1997).
- 201 5. H. Stommel, Thermohaline convection with two stable regimes of flow. *Tellus* **13**, 224-
202 230 (1961).
- 203 6. T. F. Stocker, D. G. Wright, Rapid transitions of the ocean's deep circulation induced
204 by changes in surface water fluxes. *Nature* **351**, 729-732 (1991).
- 205 7. M. Hofmann, S. Rahmstorf, On the stability of the Atlantic meridional overturning
206 circulation. *Proc. Natl. Acad. Sci. U.S.A.* **106**, 20584-20589 (2009).
- 207 8. M. Srokosz, H. Bryden, Observing the Atlantic Meridional Overturning Circulation
208 yields a decade of inevitable surprises. *Science* **348**, 1255575 (2015).
- 209 9. M. Lozier *et al.*, A sea change in our view of overturning in the subpolar North
210 Atlantic. *Science* **363**, 516-521 (2019).
- 211 10. E. V. Galaasen *et al.*, Rapid Reductions in North Atlantic Deep Water During the Peak
212 of the Last Interglacial Period. *Science* **343**, 1129-1132 (2014).

- 213 11. J. F. Adkins, E. A. Boyle, L. Keigwin, E. Cortijo, Variability of the North Atlantic
214 thermohaline circulation during the last interglacial period. *Nature* **390**, 154-156
215 (1997).
- 216 12. H. K. F. Kleiven *et al.*, Reduced North Atlantic Deep Water coeval with the glacial
217 Lake Agassiz freshwater outburst. *Science* **319**, 60-64 (2008).
- 218 13. J. F. McManus, D. W. Oppo, J. L. Cullen, A 0.5-million-year record of millennial-scale
219 climate variability in the North Atlantic. *Science* **283**, 971-975 (1999).
- 220 14. D. W. Oppo, J. F. McManus, J. L. Cullen, Abrupt climate events 500,000 to 340,000
221 years ago: Evidence from subpolar North Atlantic sediments. *Science* **279**, 1335-1338
222 (1998).
- 223 15. D. A. Hodell *et al.*, Surface and deep-water hydrography on Gardar Drift (Iceland
224 Basin) during the last interglacial period. *Earth Planet. Sci. Lett.* **288**, 10-19 (2009).
- 225 16. A. de Vernal, C. Hillaire-Marcel, Natural variability of Greenland climate, vegetation,
226 and ice volume during the past million years. *Science* **320**, 1622-1625 (2008).
- 227 17. A. Berger *et al.*, Interglacials of the last 800,000 years. *Reviews of Geophysics* **54**, 162-
228 219 (2016).
- 229 18. A. V. Reyes *et al.*, South Greenland ice-sheet collapse during Marine Isotope Stage 11.
230 *Nature* **510**, 525-528 (2014).
- 231 19. See the supplementary materials.
- 232 20. A. Schmittner *et al.*, Calibration of the carbon isotope composition ($\delta^{13}\text{C}$) of benthic
233 foraminifera. *Paleoceanography* **32**, 512-530 (2017).

- 234 21. B. Corliss, X. Sun, C. Brown, W. Showers, Influence of seasonal primary productivity
235 on $\delta^{13}\text{C}$ of North Atlantic deep-sea benthic foraminifera. *Deep Sea Research Part I:*
236 *Oceanographic Research Papers* **53**, 740-746 (2006).
- 237 22. M. Eide, A. Olsen, U. S. Ninnemann, T. Johannessen, A global ocean climatology of
238 preindustrial and modern ocean $\delta^{13}\text{C}$. *Global Biogeochem. Cycles* **31**, 515-534 (2017).
- 239 23. L. E. Lisiecki, M. E. Raymo, W. B. Curry, Atlantic overturning responses to Late
240 Pleistocene climate forcings. *Nature* **456**, 85-88 (2008).
- 241 24. L. Henry *et al.*, North Atlantic ocean circulation and abrupt climate change during the
242 last glaciation. *Science* **353**, 470-474 (2016).
- 243 25. N. Bouttes, D. Roche, V. Mariotti, L. Bopp, Including an ocean carbon cycle model
244 into iLOVECLIM (v1. 0). *Geoscientific Model Development* **8**, 1563-1576 (2015).
- 245 26. J. F. McManus, R. Francois, J. M. Gherardi, L. D. Keigwin, S. Brown-Leger, Collapse
246 and rapid resumption of Atlantic meridional circulation linked to deglacial climate
247 changes. *Nature* **428**, 834-837 (2004).
- 248 27. R. Ferrari *et al.*, Antarctic sea ice control on ocean circulation in present and glacial
249 climates. *Proc. Natl. Acad. Sci. U.S.A.* **111**, 8753-8758 (2014).
- 250 28. G. Vettoretti, W. R. Peltier, Fast Physics and Slow Physics in the Nonlinear
251 Dansgaard–Oeschger Relaxation Oscillation. *J. Clim.* **31**, 3423-3449 (2018).
- 252 29. B. Martrat *et al.*, Four climate cycles of recurring deep and surface water
253 destabilizations on the Iberian margin. *Science* **317**, 502-507 (2007).
- 254 30. C. R. W. Ellison, M. R. Chapman, I. R. Hall, Surface and deep ocean interactions
255 during the cold climate event 8200 years ago. *Science* **312**, 1929-1932 (2006).

- 256 31. J. A. L. Nicholl *et al.*, A Laurentide outburst flooding event during the last interglacial
257 period. *Nat. Geosci.* **5**, 901-904 (2012).
- 258 32. R. G. Hatfield *et al.*, Interglacial responses of the southern Greenland ice sheet over the
259 last 430,000 years determined using particle-size specific magnetic and isotopic tracers.
260 *Earth Planet. Sci. Lett.* **454**, 225-236 (2016).
- 261 33. M. E. Raymo *et al.*, Stability of North Atlantic water masses in face of pronounced
262 climate variability during the Pleistocene. *Paleoceanography* **19**, PA2008 (2004).
- 263 34. L. E. Lisiecki, M. E. Raymo, A Pliocene-Pleistocene stack of 57 globally distributed
264 benthic $\delta^{18}\text{O}$ records. *Paleoceanography* **20**, PA1003 (2005).
- 265 35. J. Laskar *et al.*, A long-term numerical solution for the insolation quantities of the
266 Earth. *Astronomy and Astrophysics* **428**, 261-285 (2004).
- 267 36. E. J. Colville *et al.*, Sr-Nd-Pb isotope evidence for ice-sheet presence on southern
268 Greenland during the last interglacial. *Science* **333**, 620-623 (2011).
- 269 37. L. E. Lisiecki, A simple mixing explanation for late Pleistocene changes in the Pacific-
270 South Atlantic benthic $\delta^{13}\text{C}$ gradient. *Clim. Past* **6**, 305-314 (2010).
- 271 38. C. Xuan, J. E. T. Channell, D. A. Hodell, Quaternary magnetic and oxygen isotope
272 stratigraphy in diatom-rich sediments of the southern Gardar Drift (IODP Site U1304,
273 North Atlantic). *Quat. Sci. Rev.* **142**, 74-89 (2016).
- 274 39. C. Hillaire-Marcel, A. de Vernal, J. McKay, Foraminifer isotope study of the
275 Pleistocene Labrador Sea, northwest North Atlantic (IODP Sites 1302/03 and 1305),
276 with emphasis on paleoceanographical differences between its “inner” and “outer”
277 basins. *Mar. Geol.* **279**, 188-198 (2011).

- 278 40. D. A. Hodell, J. H. Curtis, Oxygen and carbon isotopes of detrital carbonate in North
279 Atlantic Heinrich Events. *Mar. Geol.* **256**, 30-35 (2008).
- 280 41. Y. Rosenthal, M. P. Field, R. M. Sherrell, Precise determination of element/calcium
281 ratios in calcareous samples using sector field inductively coupled plasma mass
282 spectrometry. *Anal. Chem.* **71**, 3248-3253 (1999).
- 283 42. N. Irvall *et al.*, A low climate threshold for south Greenland Ice Sheet demise during
284 the Late Pleistocene. *Proc. Natl. Acad. Sci. U.S.A.* **117**, 190-195 (2020).
- 285 43. H. Goosse *et al.*, Description of the Earth system model of intermediate complexity
286 LOVECLIM version 1.2. *Geoscientific Model Development* **3**, 603-633 (2010).
- 287 44. F. J. Millero, Thermodynamics of the carbon dioxide system in the oceans. *Geochimica
288 et Cosmochimica Acta* **59**, 661-677 (1995).
- 289 45. S. Barker *et al.*, Icebergs not the trigger for North Atlantic cold events. *Nature* **520**, 333
290 (2015).
- 291 46. L. C. Skinner, N. J. Shackleton, Deconstructing Terminations I and II: revisiting the
292 glacioeustatic paradigm based on deep-water temperature estimates. *Quat. Sci. Rev.* **25**,
293 3312-3321 (2006).
- 294 47. H. F. Evans *et al.*, Paleointensity-assisted chronostratigraphy of detrital layers on the
295 Eirik Drift (North Atlantic) since marine isotope stage 11. *Geochem. Geophys. Geosyst*
296 **8**, (2007).
- 297 48. C. Hillaire-Marcel, A. Vernal, G. Bilodeau, G. Wu, Isotope stratigraphy, sedimentation
298 rates, deep circulation, and carbonate events in the Labrador Sea during the last ~200
299 ka. *Canadian Journal of Earth Sciences* **31**, 63-89 (1994).

- 300 49. J. S. Stoner, J. E. Channell, C. Hillaire-Marcel, The magnetic signature of rapidly
301 deposited detrital layers from the deep Labrador Sea: Relationship to North Atlantic
302 Heinrich layers. *Paleoceanography* **11**, 309-325 (1996).
- 303 50. A. E. Carlson, J. S. Stoner, J. P. Donnelly, C. Hillaire-Marcel, Response of the southern
304 Greenland Ice Sheet during the last two deglaciations. *Geology* **36**, 359-362 (2008).
- 305 51. J. Yu, H. Elderfield, Benthic foraminiferal B/Ca ratios reflect deep water carbonate
306 saturation state. *Earth Planet. Sci. Lett.* **258**, 73-86 (2007).
- 307 52. J. Yu, H. Elderfield, A. M. Piotrowski, Seawater carbonate ion- $\delta^{13}\text{C}$ systematics and
308 application to glacial–interglacial North Atlantic ocean circulation. *Earth Planet. Sci.*
309 *Lett.* **271**, 209-220 (2008).
- 310 53. T. Fronval, E. Jansen, H. Hafliðason, H. P. Sejrup, Variability in surface and deep
311 water conditions in the nordic seas during the last interglacial period. *Quat. Sci. Rev.*
312 **17**, 963-985 (1998).
- 313 54. J. E. T. Channell *et al.*, *Expedition 303 Summary*. Proceeding of the Integrated Ocean
314 Drilling Program (Integrated Ocean Drilling Program Management International Inc.,
315 2006), vol. 303/306. doi:10.2204/iodp.proc.303306.101.2006
- 316 55. N. Irválı *et al.*, Rapid switches in subpolar North Atlantic hydrography and climate
317 during the Last Interglacial (MIS 5e). *Paleoceanography* **27**, PA2207 (2012).
- 318 56. C. Laj, X. Morin, the Shipboard Scientific Party, MD132-P.I.C.A.S.S.O/IMAGES XI
319 cruise report, Les rapports de campagne à la mer, No. *OCE/2004/02* (Plouzané, France,
320 2004).
- 321 57. K. E. Kohfeld, R. G. Fairbanks, S. L. Smith, I. D. Walsh, Neogloboquadrina
322 pachyderma (sinistral coiling) as paleoceanographic tracers in polar oceans: Evidence

323 from Northeast Water Polynya plankton tows, sediment traps, and surface sediments.
324 *Paleoceanography* **11**, 679-699 (1996).

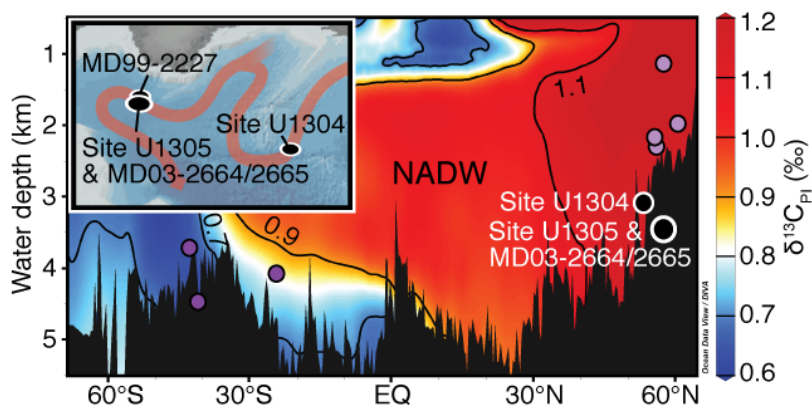
325

326 **Acknowledgments:** We thank the scientific party and crew of R/V *JOIDES Resolution* IODP
327 Expedition 303, the curatorial staff at the IODP Bremen core repository for core sampling
328 assistance, and Douglas Richmond for assistance with processing MIS 9e samples. **Funding:**
329 Funded by grants from the Research Council of Norway (RCN) through the project
330 THRESHOLDS (RCN grant 254964) and data generation at FARLAB (RCN grant 245907).
331 **Author contributions:** U.S.N. and E.V.G. designed the project and all co-authors helped
332 conceptualize the study; E.V.G. processed the sediment samples and conducted the benthic and
333 planktic foraminifera stable isotope analyses; N.I. conducted the IRD analyses; A.K., J.T.,
334 N.B., and D.M.R. designed and performed the iLOVECLIM simulation; Y.R. performed the
335 B/Ca analyses; E.V.G. led the writing effort and coordinated input from all co-authors.
336 **Competing interests:** None declared. **Data and materials availability:** The data are available
337 in the Supplementary Materials.

338

339 **Supplementary Materials:**

340 Materials and Methods
341 Supplementary text
342 Figures S1-S7
343 References (39-57)

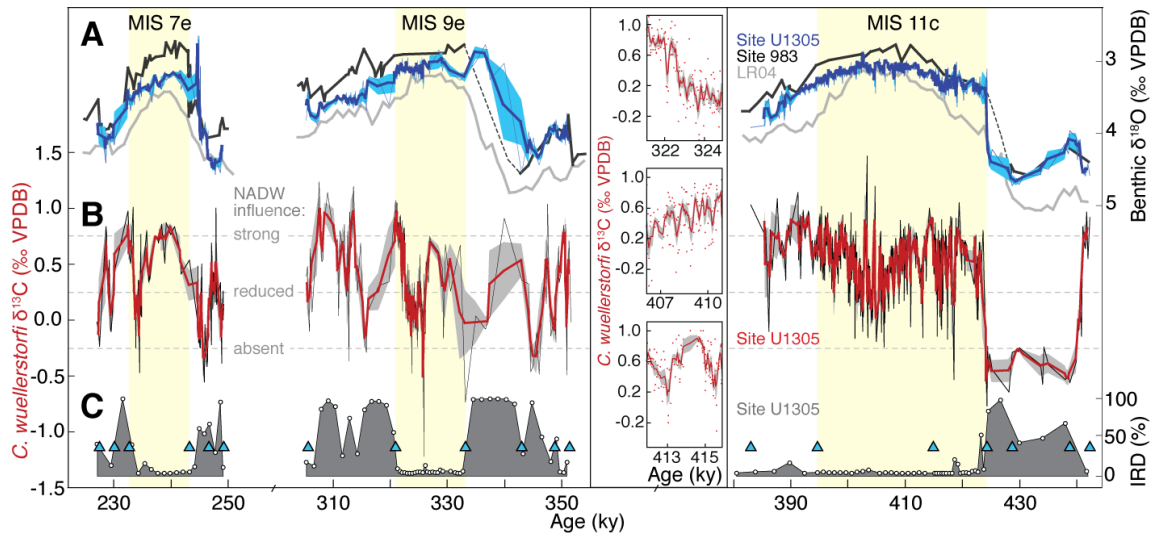


344

345 **Fig. 1. Core locations.** IODP Site U1305 (57°29'N, 48°32'W; 3459 m), MD03-2664
 346 (57°26'N, 48°36'W; 3442 m), MD03-2665 (57°26'N, 48°36'W; 3440 m), and IODP Site
 347 U1304 (53°03'N, 33°32'W; 3082 m) projected on a western Atlantic north-south section of
 348 preindustrial $\delta^{13}\text{C}$ ($\delta^{13}\text{C}^{\text{PI}}$) (22) plotted using Ocean Data View. Core sites depicted in the data
 349 composites of Fig. 3C are included (light and dark purple circles). Inset, plotted using
 350 GeoMapApp, shows the key subpolar core sites including MD99-2227 (58°21'N, 48°37'W;
 351 3460 m) and the main spreading pathways of Nordic Seas-sourced deep water contributing to
 352 lower NADW (red).

353

354



355

356 **Fig. 2. IODP Site U1305 MIS 7e, 9e, and 11c *C. wuellerstorfi* stable isotope and ice-rafting**

357 **records.** A) Benthic $\delta^{18}\text{O}$ from IODP Site U1305 (thin blue line, sample average of replicate

358 measurements; bold dark blue, 3-point running mean; shading, the standard error of the 3-point

359 lines denote prolonged gaps) (33), and LR04 for reference (gray) (34); B) Site U1305 *C.*

360 *wuellerstorfi* $\delta^{13}\text{C}$ (black, sample average; red, 3-point running mean; shading, standard error

361 of 3-point window) with dashed vertical lines denoting approximate levels of NADW

362 influence; C) position of age model tie points (triangles) and Site U1305 ice-rafted debris

363 (IRD; % of >150 μm entities; black and gray) (19). All records are on the LR04 timescale (19).

364 The sample spacing gives the benthic stable isotope records a nominal time resolution of 70

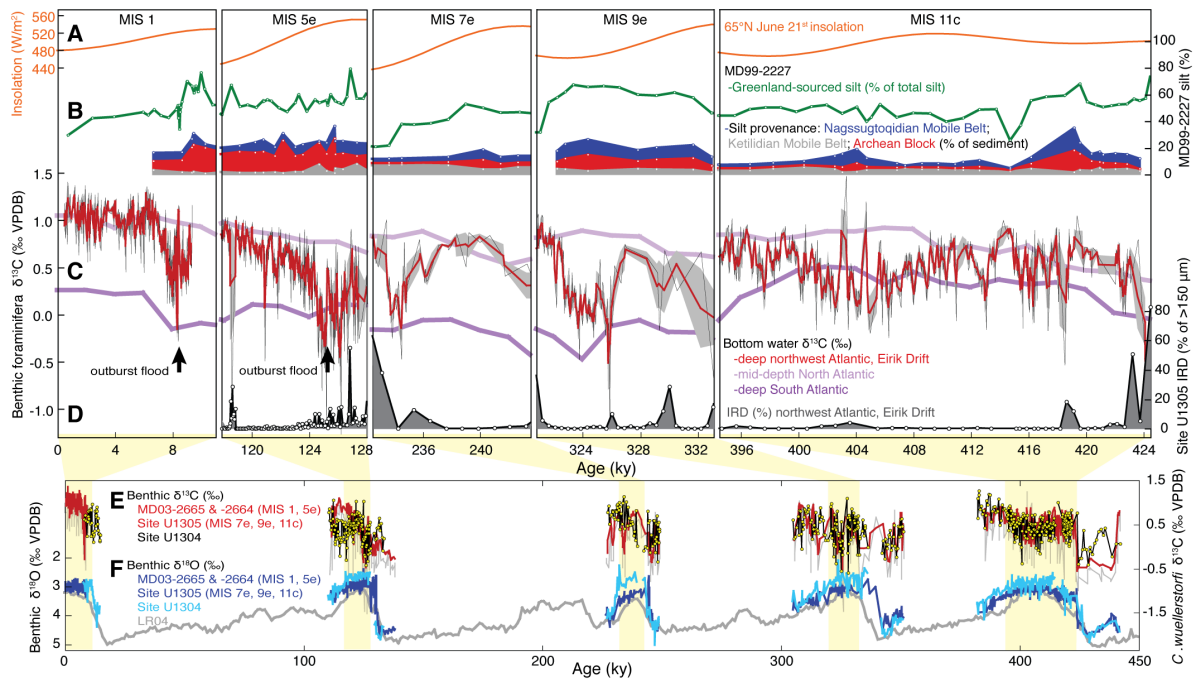
365 years during the interglacial benthic $\delta^{18}\text{O}$ plateaus (shaded yellow). Insets show examples of

366 the *C. wuellerstorfi* $\delta^{13}\text{C}$ variability (coloring as in B, individual data as dots). VPDB, Vienna

367 Pee Dee Belemnite standard.

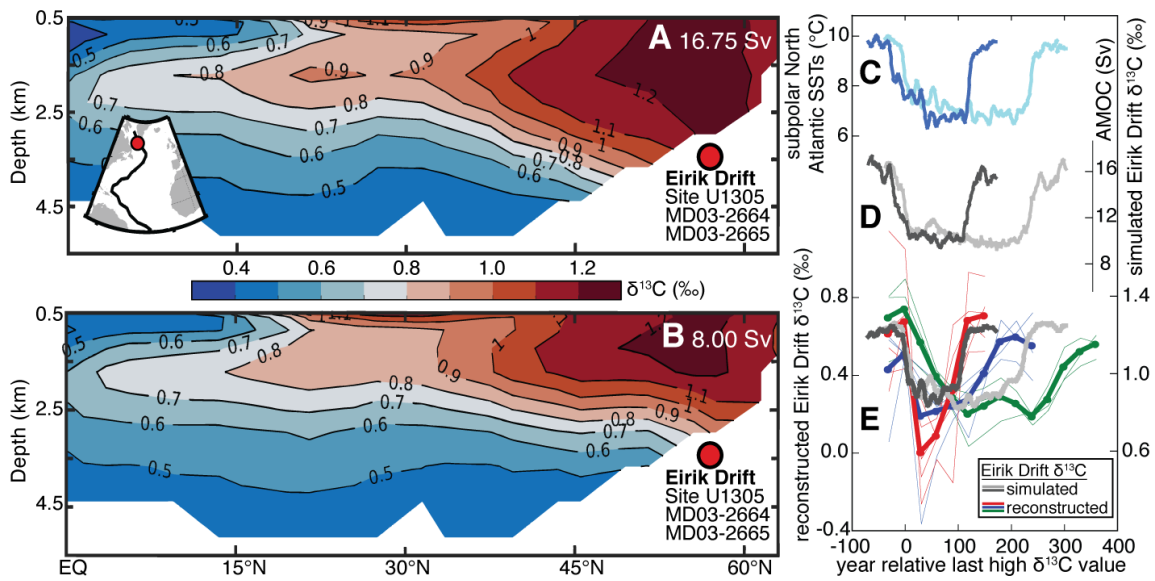
368

369



370

371 **Fig. 3. Variability in NADW ventilation during interglacials MIS 1-11c.** Focused on the
 372 interglacial $\delta^{18}\text{O}$ plateaus: A) 65°N insolation at June 21st (orange) (35); B) core MD99-2227
 373 records of GrIS sediment discharge showing silt sourced from Precambrian Greenland terranes
 374 (green, % of total silt) (32) and from different Greenland provenances (% of sediment: colored,
 375 see text inset) (18, 32, 36); C) bottom water $\delta^{13}\text{C}$ reconstructions from mid-depth North (light
 376 purple) (23) and deep South Atlantic composites (dark purple) (37) (see Fig. 1 for locations),
 377 and from the deep Eirik Drift (MIS 1: 12; MIS 5e: 10; MIS 7e, 9e, and 11c: this study)
 378 (coloring as in Fig. 2) with arrows denoting freshwater outburst floods as determined in (10,
 379 12); and D) Eirik Drift ice-rafted debris (IRD) records (MIS 5e: 10; MIS 7e, 9e, and 11c: 19).
 380 Glacial-interglacial records of: E) *C. wuellerstorfi* $\delta^{13}\text{C}$ from the Eirik Drift (as in C; gray line,
 381 sample average; red line, 3-point mean) and IODP Site U1304 (black and yellow, sample
 382 average) (15, 38) (note difference in resolution, U1305: ~ 70 years; U1304: ~ 300 years); F)
 383 Benthic foraminifera $\delta^{18}\text{O}$ from the Eirik Drift and Site U1304 (colored, see inset; references as
 384 for $\delta^{13}\text{C}$), and LR04 (gray) (34). All records are plotted on the LR04 timescale (19).



385

386 **Fig. 4. Modeled and reconstructed deep Atlantic $\delta^{13}\text{C}$ changes.** (Left) The iLOVECLIM
 387 simulated $\delta^{13}\text{C}$ distribution and Eirik Drift core location (red circle) along a north-south
 388 transect (inset) averaged for years with: A) strong, modern-like AMOC ($>2\sigma$; 16.75 ± 0.70 Sv
 389 mean; $n=460$ model years) and NADW distribution; and B) weaker AMOC ($<2\sigma$; 8.00 ± 0.42
 390 Sv mean; $n=63$ model years) and shoaled NADW (see (19) for details). (Right) Across two
 391 simulated NADW shoaling events (ten-year mean values): C) subpolar North Atlantic mean
 392 sea surface temperature (SST; light and dark blue); D) AMOC stream function at 27°N (light
 393 and dark gray); and E) Eirik Drift bottom water $\delta^{13}\text{C}$ changes (light and dark gray; magnitude
 394 similar for different preformed $\delta^{13}\text{C}$ values, see (19)) compared to the reconstructions by
 395 aligning at the last high $\delta^{13}\text{C}$ values. To illustrate common features that account for interglacial
 396 differences in preformed $\delta^{13}\text{C}$ values, the reconstructed events are shown as the average (bold
 397 lines) of multiple events (thin lines) at 30-year steps (obtained by linear interpolation) binned
 398 according to durations of ≤ 100 (red; $n=5$), 101-200 (blue; $n=4$), and 201-300 years (green;
 399 $n=3$).

400

401
402
403
404
405
406
407
408
409
410
411
412
413
414
415
416
417
418
419
420
421
422
423
424
425
426
427
428
429
430

Supplementary Materials for

Interglacial instability of North Atlantic Deep Water ventilation

Eirik Vinje Galaasen, Ulysses S. Ninnemann, Augustin Kessler, Nil Irvani, Yair Rosenthal,
Jerry Tjiputra, Nathaëlle Bouttes, Didier M. Roche, Helga (Kikki) F. Kleiven, David A.
Hodell.

Correspondence to: eirik.galaasen@uib.no

This PDF file includes:

Materials and Methods
Supplementary Text
Figs. S1 to S7
References 39-57

Other Supplementary Materials for this manuscript include the following:

Data S1 [Eirik-Drift_MIS-7e-9e-11c.xlsx]

431 **Materials and Methods**432 Sample processing and *C. wuellerstorfi* stable isotopes

433 The International Ocean Drilling Program (IODP) Site U1305 intervals spanning
434 Marine Isotope Stage (MIS) 7e, 9e, and 11c were identified from the stable isotope stratigraphy
435 of Hillaire-Marcel et al. (39) and continuously subsampled at 2-cm spacing at the IODP
436 Bremen Core Repository by the curatorial staff. Bulk sediment samples were kept in deionized
437 water on a shaker for 12 hours for disaggregation before being wet sieved using a 63 μm mesh
438 sieve to separate the fine (<63 μm) and coarse fraction material (>63 μm). Following wet
439 sieving, samples were dried at 50°C.

440 Epibenthic foraminifera *Cibicidoides wuellerstorfi* (*sensu stricto*) shells (Fig. S1) were
441 selectively picked from the >150 μm sediment fraction for stable isotope analyses. The stable
442 isotope analyses were performed at the Facility for advanced isotopic research and monitoring
443 of weather, climate and biogeochemical cycling (FARLAB), Department of Earth Science,
444 University of Bergen, Norway, on a Finnigan MAT 253 mass spectrometer coupled to an
445 automated Kiel IV preparation line kept at constant 70°C. Measurements were performed on
446 one to three individual *C. wuellerstorfi* shells, depending on availability and size, and
447 duplicated per sample when possible (~64% of the samples analyzed). Fig. S2 shows the *C.*
448 *wuellerstorfi* stable isotope results from Site U1305 including all individual data points. We
449 used Carrera Marble (CM12) as a working standard measured parallel to the foraminifera
450 samples, and all values are reported relative Vienna Pee Dee Belemnite (VPDB) calibrated
451 using National Bureau of Standards (NBS) standard NBS 19 and NBS 18. The long-term
452 reproducibility (1σ) of in-house standards over the analysis period was $\leq 0.08\text{‰}$ and $\leq 0.04\text{‰}$
453 for $\delta^{18}\text{O}$ and $\delta^{13}\text{C}$, respectively. The standard cleaning step for foraminiferal stable isotope
454 analyses, involving methanol and ultrasonication, was avoided to retain mass and increase the
455 number of measurements possible, as *C. wuellerstorfi* shells were generally few and small in
456 size, often providing a total weight at the lower limit possible for analysis (~10-15 μg). Instead
457 of performing the standard cleaning step, *C. wuellerstorfi* tests were visually cleaned using a
458 brush and deionized water ('brush-cleaned') to remove any foreign material on or within them
459 prior to stable isotope analyses. To test the impact of omitting the standard cleaning step, we
460 measured surplus shells from samples (n=22) containing sufficient mass that were cleaned
461 following standard protocols ('standard-cleaned') for removing fine-grained material: adding
462 methanol to reaction vials containing the shells and keeping them in an ultrasonic bath for 10
463 seconds before extracting the methanol. The $\delta^{18}\text{O}$ and $\delta^{13}\text{C}$ values of the 'standard-cleaned' *C.*
464 *wuellerstorfi* tests are very similar to the sample average of the 'brush-cleaned' tests (Fig. S1).
465 Further, the intra-sample reproducibility of the 'brush-cleaned' Site U1305 *C. wuellerstorfi*
466 $\delta^{18}\text{O}$ and $\delta^{13}\text{C}$ data is similar to a large data set of exclusively 'standard-cleaned' *C.*
467 *wuellerstorfi* shells from the same region (the MIS 5e section of MD03-2664; location shown
468 in Fig. 1) (Fig. S1). This indicates that the visual 'brush-cleaning' and 'standard-cleaning' steps
469 performed similarly well with no discernible difference in the stable isotope values or in the
470 intra-sample variability. Nonetheless, performing the standard cleaning step for foraminiferal
471 stable isotope analyses is highly recommended when possible. Indeed, in certain regions and
472 time intervals, a cleaning procedure more stringent than the standard one is likely required to
473 accurately determine foraminiferal stable isotope values (40).

474
475 *C. wuellerstorfi* B/Ca

476 We measured B/Ca ratios in *C. wuellerstorfi* tests from intervals in MD03-2664 (MIS
477 5e) and Site U1305 (MIS 7e, 9e, and 11c). To obtain sufficient mass for B/Ca analyses (~250-
478 300 μg), and due to scarcity of *C. wuellerstorfi* tests in these sediments, it was often necessary
479 to combine tests from up to a maximum of six adjacent samples (or 12 cm of core) that we
480 restricted according to consistent *C. wuellerstorfi* $\delta^{13}\text{C}$ values. Following the selective picking,
481 the *C. wuellerstorfi* tests were opened using clean glass slides and transferred into acid-leached
482 vials. The *C. wuellerstorfi* tests were subsequently cleaned for contaminating phases, including
483 clay removal, reductive and oxidative steps, a weak acid leach, and dissolution in dilute HNO_3 .
484 The B/Ca analyses were performed using the method outlined in Rosenthal et al. (41) on a
485 Finnigan MAT Element XR Sector Field Inductively Coupled Plasma Mass Spectrometer
486 (ICP-MS) at the ICP-MS laboratory at the Institute of Marine and Coastal Sciences, Rutgers,
487 The State University of New Jersey, USA.

488
489 Site U1305 *N. pachyderma* (s) $\delta^{13}\text{C}$ records
490 *N. pachyderma* (s) tests were selectively picked from the 150-212 μm sediment fraction
491 at continuous 4-cm spacing across MIS 7e, 9e, and 11c (with notable gaps only in MIS 9e due
492 to scarcity of *N. pachyderma* (s) tests). Prior to the stable isotope analyses, the tests were
493 cleaned by adding methanol to the sample kept in reaction vials and ultrasonicated them for
494 ten seconds before removing the supernatant. The stable isotope analyses were performed at
495 FARLAB, University of Bergen, Norway, as outlined for benthic foraminifera *C. wuellerstorfi*
496 above, and with identical standard reproducibility. Measurements on *N. pachyderma* (s) were
497 replicated whenever possible (~92% of the samples), and each individual measurement was
498 performed on 6-10 individual *N. pachyderma* (s) tests.

499 Ice-rafted debris

500 The ice-rafted debris (IRD) counts were performed on the same Site U1305 samples as
501 the benthic foraminiferal stable isotope measurements, but at lower sampling density. IRD
502 counts were performed at 32-cm spacing for MIS 7e and 11c, and 16-cm spacing for MIS 9e
503 (42). Following the sample processing steps outlined above, material in the $>150\ \mu\text{m}$ fraction
504 were split, IRD grains visually identified, and IRD calculated as the percent of ≥ 300 counted
505 entities.

506 Hole U1305C MIS 11c mcd fine-tuning

507 Sediment physical properties (e.g., magnetic susceptibility) indicated cm-scale offsets
508 between Hole U1305C and the original (Hole A & B) splice over ~74.5-78.5 mcd (Fig. S3A),
509 corresponding to most of MIS 11c. We fine-tuned the mcd scale for the Hole U1305C MIS 11c
510 interval using magnetic susceptibility, shifting it between -3 cm and -19 cm to align the
511 physical property records (Fig. S3B), and include both the original and corrected core depth
512 scales in the MIS 11c data table.

513 iLOVECLIM model simulation

514 We used the iLOVECLIM Earth system model of intermediate complexity to simulate
515 and assess potential relationships between NADW distribution, northwest Atlantic bottom
516 water $\delta^{13}\text{C}$, and AMOC. The iLOVECLIM model is an isotope-enabled development branch of
517 LOVECLIM version 1.2 (43) and includes an ocean component (CLIO) with 20 vertical layers
518 and 3° by 3° horizontal resolution as well as land and ocean carbon cycle modules (25). We

522 performed a transient simulation for 125-115 ky (corresponding to MIS 5e) using annually
523 interpolated greenhouse gas and orbital forcings following the third phase of the Paleoclimate
524 Modelling Intercomparison Project (PMIP; <https://pmip3.lsce.ipsl.fr/>), initialized from a quasi-
525 equilibrium spin up of 5000 years forced with constant 125 ky boundary conditions. We
526 performed two quasi-equilibrium spin-ups prior to the 125-115 ky simulation, each integrated
527 for 5000 years. The first is based on preindustrial conditions and the second on 125 ky
528 boundary conditions. The preindustrial simulation was used to validate and confirm that
529 iLOVECLIM reproduces the spatial distribution of preindustrial ocean $\delta^{13}\text{C}$ (22), and the 125
530 ky spin-up to initialize the 125-115 transient simulation. To test the sensitivity of the simulated
531 deep Atlantic $\delta^{13}\text{C}$ variability to changes in surface biological processes and preformed $\delta^{13}\text{C}$
532 values, we ran to additional 125-115 ky transient simulations using similar initial conditions as
533 above but starting at 125 ky with either: 1) atmospheric $\delta^{13}\text{C}$ fixed at value decreased by
534 $\sim 0.6\text{‰}$ (at -7.1‰); or 2) with 50% decreased primary productivity in the modeled convection
535 regions off southern Greenland and in the Nordic Seas. We expand on the model results in the
536 discussion section of the supplement below.

537 The modeled inorganic carbon cycle is represented by dissolved inorganic carbon
538 (DIC) and alkalinity (ALK), while the organic carbon cycle includes phytoplankton,
539 zooplankton, dissolved organic carbon (DOC), slow dissolved organic carbon (DOCs),
540 particulate organic carbon (POC), and CaCO_3 . The phytoplankton is partially remineralized as
541 it sinks through the water column, while all the POC and CaCO_3 is remineralized at depth. The
542 remineralization profile follows an exponential law, adjusted to have less remineralization in
543 the upper layers and more at depth. Carbon fractionation during photosynthesis fixes ^{12}C in the
544 organic matter, which is added back by the remineralization process at depth. At the air-sea
545 interface, the carbon flux is computed from the CO_2 partial pressure difference between the
546 atmosphere and ocean at a constant gas exchange coefficient of $0.06 \text{ mol m}^{-2} \text{ yr}^{-1}$, where sea
547 surface pCO_2 is a function of temperature, salinity, DIC, and ALK following Millero (44). The
548 modeled $\delta^{13}\text{C}$ distribution is thus affected by air-sea gas exchange and organic matter
549 production/remineralization, and transported by the advection-diffusion scheme of the model.
550 Unlike ^{12}C , the atmospheric ^{13}C is prognostically simulated in response to land and ocean
551 processes.

552

553 **Supplementary Text** 554 Site U1305 age model

555 The age models for the MIS 7e, 9e, and 11c intervals of Site U1305 were constructed
556 by correlating our benthic $\delta^{18}\text{O}$ record to and adopting the age model constructed for ODP Site
557 983 (33, 45) (Fig. 2, Fig. S4). Using Site 983 benthic $\delta^{18}\text{O}$ as a tuning target has advantages
558 over other reference records. First, Site U1305 shares well-defined structures in benthic $\delta^{18}\text{O}$
559 with Site 983 (Fig. 2; Fig. S4) allowing relatively robust correlation. Further, high-resolution
560 IRD records are available from both sites and allow us to validate the benthic $\delta^{18}\text{O}$ -correlation
561 near deglacial intervals where Site U1305 benthic $\delta^{18}\text{O}$ data were often lacking due to *C.*
562 *wuellerstorfi* absence (Fig. 2). Tie points were defined based on major benthic $\delta^{18}\text{O}$ transitions
563 and linearly interpolated between to obtain ages for all core depths (Fig. S4). The Site U1305
564 and MD03-2664 IRD records were also used to guide the determination of tie points at the start
565 of the interglacial $\delta^{18}\text{O}$ plateaus, as deglacial IRD increases are observed to coincide with
566 transient decreases in benthic $\delta^{18}\text{O}$ values before MIS 5e (10) and MIS 7e, 9e, and 11c in this

567 region (Fig. 2; Fig. S4). Given their transient nature and co-occurrence with deglacial IRD,
568 these deglacial benthic $\delta^{18}\text{O}$ reductions may reflect contamination from low- $\delta^{18}\text{O}$ detrital
569 carbonate commonly deposited during Heinrich-events (40). Consequently, deglacial samples
570 with low *C. wuellerstorfi* $\delta^{18}\text{O}$ and high IRD were disregarded when we constructed our age
571 model and we defined the first interglacial benthic $\delta^{18}\text{O}$ value, and start of the interglacial
572 plateaus, as the first continuously low $\delta^{18}\text{O}$ value occurring after large deglacial IRD increases.
573 Corroborating this approach, the Site U1305/MD03-2664 and Site 983 deglacial IRD peaks
574 align using this additional constraint for the benthic $\delta^{18}\text{O}$ tuning (Fig. S4) but would otherwise
575 be offset by a few thousand years.

576 Age uncertainties involved with benthic $\delta^{18}\text{O}$ -based age models can be considerable.
577 For example, age differences between major $\delta^{18}\text{O}$ transitions can reach up to a few thousand
578 years between different ocean basins (46). The absolute age uncertainty provided by the Site
579 U1305-Site 983 correlation is likely less than millennial, given i) the relative proximity of
580 these core sites, ii) the similarity of the benthic $\delta^{18}\text{O}$ records—indicating a shared $\delta^{18}\text{O}$
581 evolution, and iii) the alignment of deglacial IRD peaks (Fig. 2; Fig. S4). Despite a relatively
582 robust correlation, the original age model still carries considerable uncertainty in absolute ages.
583 For example, adopting a different age model constructed for Site 983 by Barker et al. (45) (e.g.,
584 EDC3 and AICC2012), would shift absolute ages up to a few thousand years.

585 In addition to absolute age uncertainties, relative (sample-to-sample) age uncertainties
586 likely also exist for the Eirik Drift (Site U1305 and MD03-2664) records. Correlation of
587 benthic $\delta^{18}\text{O}$ records is achieved using a limited number of tie points. This is especially true for
588 interglacial $\delta^{18}\text{O}$ plateaus, here defined by two (MIS 5e, 7e, and 9e) or three (MIS 11c) tie
589 points (Fig. 2, Fig. S4). These tie points were linearly interpolated between, assuming constant
590 sedimentation rates. However, interglacial sedimentation rates can vary on a range of
591 timescales in this area (39, 47-49). For example, radiocarbon-dated sections indicate that
592 sedimentation rates were higher in the early compared to the late phase of the current
593 interglacial at multiple Eirik Drift locations (e.g., 12, 48). If this temporal sedimentation pattern
594 persisted in the older interglacial periods, our age models based on the conservative approach
595 of linear interpolation may over- and underestimate the durations of early and late interglacial
596 intervals, respectively.

597 Site U1304, MD03-2664, MD03-2665, and MD99-2227 age models

599 To place all proxy records on a common age scale, we revised the age models for all
600 core intervals containing data we compare to the IODP Site U1305 records. We tuned the MIS
601 5e interval of MD03-2664 and the MIS 5e, 7e, 9e, and 11c intervals of IODP Site U1304 to the
602 same ODP Site 983 reference record (Fig. S4), applying identical tie points and linearly
603 interpolating between as outlined above. The MIS 1 and last deglacial intervals of Site U1304
604 and MD03-2665 were left on their original age models as presented in Xuan et al. (38) and
605 Kleiven et al. (12), respectively.

606 To compare our records to the MD99-2227 southern Greenland sediment discharge
607 reconstructions (18, 32, 36), we transferred our benthic $\delta^{18}\text{O}$ -based age models for MIS 5e
608 (MD03-2664), 7e, 9e, and 11c (Site U1305) to MD99-2227 by correlating magnetic
609 susceptibility between this core and MD03-2664 (MIS 5e) and Site U1305 (MIS 7e, 9e, and
610 11c) (Fig. S5). The strong similarity of the magnetic susceptibility records indicate that these
611 core sites shared sedimentation histories, providing robust relative age control to comparisons
612 of the Site U1305/MD03-2664 and MD99-2227 records. The alignment of glacial and

613 interglacials values in epibenthic foraminifera *C. wuellerstorfi* $\delta^{18}\text{O}$ from MD03-2664/Site
614 U1305 and planktic foraminifera *N. pachyderma* (s) $\delta^{18}\text{O}$ from MD99-2227 on the obtained
615 age models supports the magnetic susceptibility correlation (Fig. S5). Carlson et al.'s (50) age
616 model was used for the MIS 1 and last deglacial intervals of MD99-2227.

617
618 *C. wuellerstorfi* B/Ca and *N. pachyderma* (s) $\delta^{13}\text{C}$

619 To test the fidelity of Eirik Drift *C. wuellerstorfi* $\delta^{13}\text{C}$ as recorder of bottom water
620 carbon chemistry and water mass tracer, we use epibenthic foraminifera *C. wuellerstorfi* B/Ca,
621 a proxy for bottom water carbonate ion saturation ($\Delta[\text{CO}_3^{2-}]$) and independent metric of the
622 influence of high- $[\text{CO}_3^{2-}]$ NADW versus low- $[\text{CO}_3^{2-}]$ SSW (e.g., 51, 52). The Eirik Drift *C.*
623 *wuellerstorfi* B/Ca data span a range of 185-215 $\mu\text{mol/mol}$ with distinct changes within each of
624 MIS 5e, 7e, 9e, and 11c (Fig. S6). Using Yu & Elderfield's (51) B/Ca to $\Delta[\text{CO}_3^{2-}]$ relationship
625 for *C. wuellerstorfi*, the B/Ca data indicates intra-interglacial changes in bottom water $[\text{CO}_3^{2-}]$
626 by 25-30 $\mu\text{mol/kg}$, similar to that expected from shifting between NADW and SSW influence
627 (e.g., 52). The concurrent and coupled changes in *C. wuellerstorfi* $\delta^{13}\text{C}$ by up to $\sim 0.8\text{‰}$ within
628 the same sample pool (Fig. S6) is similarly consistent with shifts between NADW and SSW
629 influence. Indeed, the paired change in Eirik Drift *C. wuellerstorfi* B/Ca and $\delta^{13}\text{C}$ we observe is
630 similar to that recorded in the last glacial to Holocene sections of two North Atlantic cores
631 from similar water depths (Fig. S6) that was previously interpreted to reflect the well-
632 established deglacial shift from SSW to NADW influence in the deep North Atlantic (52). We
633 suggest that the Eirik Drift *C. wuellerstorfi* B/Ca record supports the interpretation of the *C.*
634 *wuellerstorfi* $\delta^{13}\text{C}$ variability as reflecting changes in NADW versus SSW influence.

635 An alternative explanation for co-variability in trace element ratios and $\delta^{13}\text{C}$ is
636 contamination by secondary CaCO_3 precipitation and presence of authigenic overgrowths.
637 However, several lines of evidence argue against a role for contamination by secondary CaCO_3
638 precipitation. The *C. wuellerstorfi* $\delta^{13}\text{C}$ record suggest no discernible influence by its own
639 merit, showing for example i) absolute values within the range of values observed in the
640 modern ocean or relevant reconstructions (e.g., 22, 23; Fig. 3) and ii) a consistency in the
641 signal and a lack of extremely large fluctuations that would require the mass and isotope value
642 of any contamination to have adjusted itself to balance changes in the mass and isotope value
643 of the foraminifera tests. Further, secondary CaCO_3 precipitation should, if present, influence
644 all foraminifera tests in a given core depth to some degree similarly. That is, if secondary
645 CaCO_3 precipitation drove relatively large changes in *C. wuellerstorfi* $\delta^{13}\text{C}$ and B/Ca, planktic
646 foraminifera $\delta^{13}\text{C}$ should also show low $\delta^{13}\text{C}$ values in addition to some degree of co-
647 variability. The Eirik Drift *N. pachyderma* (s) $\delta^{13}\text{C}$ records from MIS 5e, 7e, 9e, and 11c do not
648 show values as low as the *C. wuellerstorfi* $\delta^{13}\text{C}$ records and there is no significant relationship
649 between *N. pachyderma* (s) and *C. wuellerstorfi* $\delta^{13}\text{C}$ (Fig. S6). In sum, we suggest secondary
650 CaCO_3 precipitation is either unimportant or entirely absent and consider it as an unlikely
651 explanation for the co-variability in *C. wuellerstorfi* B/Ca and $\delta^{13}\text{C}$. Changes in the influence
652 of NADW versus SSW could conversely explain these observations.

653
654 iLOVECLIM model simulation results

655 We identified persistent centennial-scale variability in $\delta^{13}\text{C}$ and the distribution of
656 NADW in our 125-115 ky transient simulation occurring over a ~ 6 ky long interval in-between
657 intervals of relative stability during the initial 2-3 and final 1-2 ky. A subsequent study will
658 outline and discuss the results of the model simulation in detail (Kessler et al., in prep.). Here,

659 we use the simulation to help the interpretation of the reconstructed bottom water $\delta^{13}\text{C}$
660 variability by assessing how centennial-scale changes in NADW distribution can impact deep
661 Atlantic $\delta^{13}\text{C}$. We focus on the simulated episodes of NADW shoaling and recovery to assess
662 the possible rate, duration, and magnitude of water mass distribution and associated bottom
663 water $\delta^{13}\text{C}$ changes and compare these to the reconstructed $\delta^{13}\text{C}$ variability. In the simulation,
664 episodes of NADW shoaling were abruptly initiated, lasted some centuries, and were
665 associated with decreases in AMOC strength and North Atlantic bottom water $\delta^{13}\text{C}$ (Fig. 4).

666 The simulated episodes of NADW shoaling/deepening produced distinct North Atlantic
667 bottom water $\delta^{13}\text{C}$ variability as (low- $\delta^{13}\text{C}$) Southern source water (SSW) expanded/contracted
668 in concert with (high- $\delta^{13}\text{C}$) NADW contracting/expanding (Fig. 4). In the northwest Atlantic
669 region corresponding to the location of Eirik Drift core sites U1305, MD03-2664, and MD03-
670 2665, shoaling of NADW and incursions of SSW manifested as $\sim 0.4\%$ decreases in bottom
671 water $\delta^{13}\text{C}$ achieved over a few decades, events that ended equally abrupt as NADW deepened
672 some centuries (~ 100 -500 years) later (Fig. 4). To illustrate these NADW and $\delta^{13}\text{C}$ distribution
673 changes, Fig. 4A and Fig. 4B displays the North Atlantic mean $\delta^{13}\text{C}$ distribution below 500 m
674 water depth for all simulated years with anomalously strong AMOC ($>2\sigma$; $n=460$ model years;
675 mean AMOC strength: 16.75 ± 0.70 Sv) and anomalously weak AMOC ($<2\sigma$; $n=63$ model
676 years; mean AMOC strength: 8.00 ± 0.42 Sv), respectively. We further selected two simulated
677 intervals of NADW shoaling and recovering to compare to the reconstructed bottom water $\delta^{13}\text{C}$
678 variability (Fig. 4B), differing from other simulated shoaling episodes only in duration. The
679 magnitude of any bottom water $\delta^{13}\text{C}$ variability driven by such changes in the relative
680 influence of northern versus southern source water could depend strongly on the preformed
681 $\delta^{13}\text{C}$ of, and the gradient between, competing water masses. While iLOVECLIM captures the
682 preindustrial preformed $\delta^{13}\text{C}$ of northern and southern source waters relatively well (e.g.,
683 compare Fig. 1 to Fig. 4A), proxy records suggest considerable changes in preformed water
684 mass $\delta^{13}\text{C}$ occurred between and even within past interglacial periods. For example, the
685 preformed $\delta^{13}\text{C}$ of northern source water may have been higher in the Holocene than the late
686 Pleistocene interglacials (see data composites, purple lines, in Fig. 3), while it likely increased
687 across MIS 5e (Fig. 3) consistent with planktic and epibenthic foraminifera $\delta^{13}\text{C}$ records from
688 the Nordic Seas (e.g., 53). This model-data difference should be noted when comparing and
689 contrasting the simulated and reconstructed time series. For the proxy reconstructions, we took
690 this into account by averaging multiple events in order to illustrate common features
691 independent of specific interglacials and preformed $\delta^{13}\text{C}$ values (Fig. 4). Still, the similarity of
692 the modeled and reconstructed bottom water $\delta^{13}\text{C}$ changes could result from the simulation
693 having a specific set of preformed $\delta^{13}\text{C}$ values in NADW and SSW. To assess how different
694 background states and preformed $\delta^{13}\text{C}$ in NADW and SSW could impact the magnitude and
695 character of the simulated bottom water $\delta^{13}\text{C}$ variability, we reran the simulation twice with 1)
696 atmospheric $\delta^{13}\text{C}$ lowered by $\sim 0.6\%$ and 2) 50% decreased primary productivity in the
697 simulated deep water formation regions off southern Greenland and in the Nordic Seas. Both
698 experiments shift the absolute values of the simulated Eirik Drift bottom water $\delta^{13}\text{C}$ time series
699 but in both cases the relative magnitudes and character of the variability is only negligibly
700 impacted (Fig. S7). The simulation with perturbed primary productivity, resulting in limited
701 change in deep Atlantic $\delta^{13}\text{C}$, supports previous studies suggesting that organic carbon fluxes
702 have little influence on the $\delta^{13}\text{C}$ of *C. wuellerstorfi* (e.g., 21). Thus, the character of the Eirik
703 Drift bottom water $\delta^{13}\text{C}$ variability driven by shifts in the distribution of water masses appears
704 to be relatively stable in face of different preformed $\delta^{13}\text{C}$ values and background biological

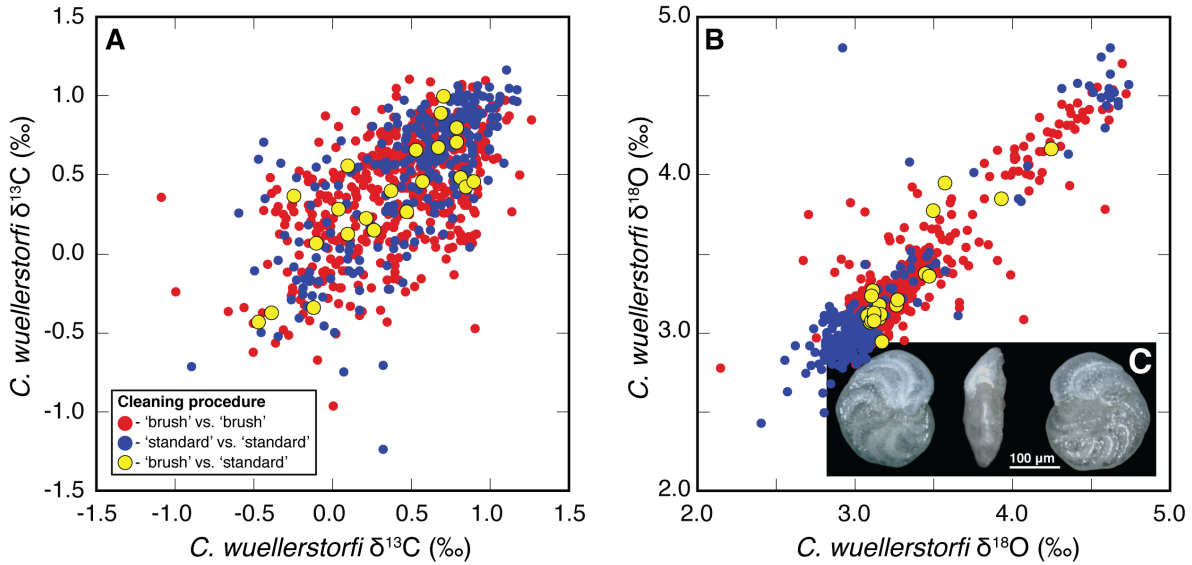
705 processes in the model, indicating that the similarity between the simulated and reconstructed
706 variability is not strongly dependent on the specific model configuration. That this character is
707 similar to the reconstructed Eirik Drift bottom water $\delta^{13}\text{C}$ reductions, including in the
708 magnitude, rate, and duration of events (Fig. 4; Fig. S7), supports the inference that
709 characteristic deep Atlantic $\delta^{13}\text{C}$ changes can be explained with changes in the distribution and
710 influence of NADW and SSW.

711

712 **References and notes**

- 713 39. C. Hillaire-Marcel, A. de Vernal, J. McKay, Foraminifer isotope study of the
714 Pleistocene Labrador Sea, northwest North Atlantic (IODP Sites 1302/03 and 1305),
715 with emphasis on paleoceanographical differences between its “inner” and “outer”
716 basins. *Mar. Geol.* **279**, 188-198 (2011).
- 717 40. D. A. Hodell, J. H. Curtis, Oxygen and carbon isotopes of detrital carbonate in North
718 Atlantic Heinrich Events. *Mar. Geol.* **256**, 30-35 (2008).
- 719 41. Y. Rosenthal, M. P. Field, R. M. Sherrell, Precise determination of element/calcium
720 ratios in calcareous samples using sector field inductively coupled plasma mass
721 spectrometry. *Anal. Chem.* **71**, 3248-3253 (1999).
- 722 42. N. Irvál *et al.*, A low climate threshold for south Greenland Ice Sheet demise during
723 the Late Pleistocene. *Proc. Natl. Acad. Sci. U.S.A.* **117**, 190-195 (2020).
- 724 43. H. Goosse *et al.*, Description of the Earth system model of intermediate complexity
725 LOVECLIM version 1.2. *Geoscientific Model Development* **3**, 603-633 (2010).
- 726 44. F. J. Millero, Thermodynamics of the carbon dioxide system in the oceans. *Geochimica
727 et Cosmochimica Acta* **59**, 661-677 (1995).
- 728 45. S. Barker *et al.*, Icebergs not the trigger for North Atlantic cold events. *Nature* **520**, 333
729 (2015).
- 730 46. L. C. Skinner, N. J. Shackleton, Deconstructing Terminations I and II: revisiting the
731 glacioeustatic paradigm based on deep-water temperature estimates. *Quat. Sci. Rev.* **25**,
732 3312-3321 (2006).
- 733 47. H. F. Evans *et al.*, Paleointensity-assisted chronostratigraphy of detrital layers on the
734 Eirik Drift (North Atlantic) since marine isotope stage 11. *Geochem. Geophys. Geosyst*
735 **8**, (2007).
- 736 48. C. Hillaire-Marcel, A. Vernal, G. Bilodeau, G. Wu, Isotope stratigraphy, sedimentation
737 rates, deep circulation, and carbonate events in the Labrador Sea during the last ~200
738 ka. *Canadian Journal of Earth Sciences* **31**, 63-89 (1994).
- 739 49. J. S. Stoner, J. E. Channell, C. Hillaire-Marcel, The magnetic signature of rapidly
740 deposited detrital layers from the deep Labrador Sea: Relationship to North Atlantic
741 Heinrich layers. *Paleoceanography* **11**, 309-325 (1996).
- 742 50. A. E. Carlson, J. S. Stoner, J. P. Donnelly, C. Hillaire-Marcel, Response of the southern
743 Greenland Ice Sheet during the last two deglaciations. *Geology* **36**, 359-362 (2008).
- 744 51. J. Yu, H. Elderfield, Benthic foraminiferal B/Ca ratios reflect deep water carbonate
745 saturation state. *Earth Planet. Sci. Lett.* **258**, 73-86 (2007).
- 746 52. J. Yu, H. Elderfield, A. M. Piotrowski, Seawater carbonate ion- $\delta^{13}\text{C}$ systematics and
747 application to glacial–interglacial North Atlantic ocean circulation. *Earth Planet. Sci.
748 Lett.* **271**, 209-220 (2008).

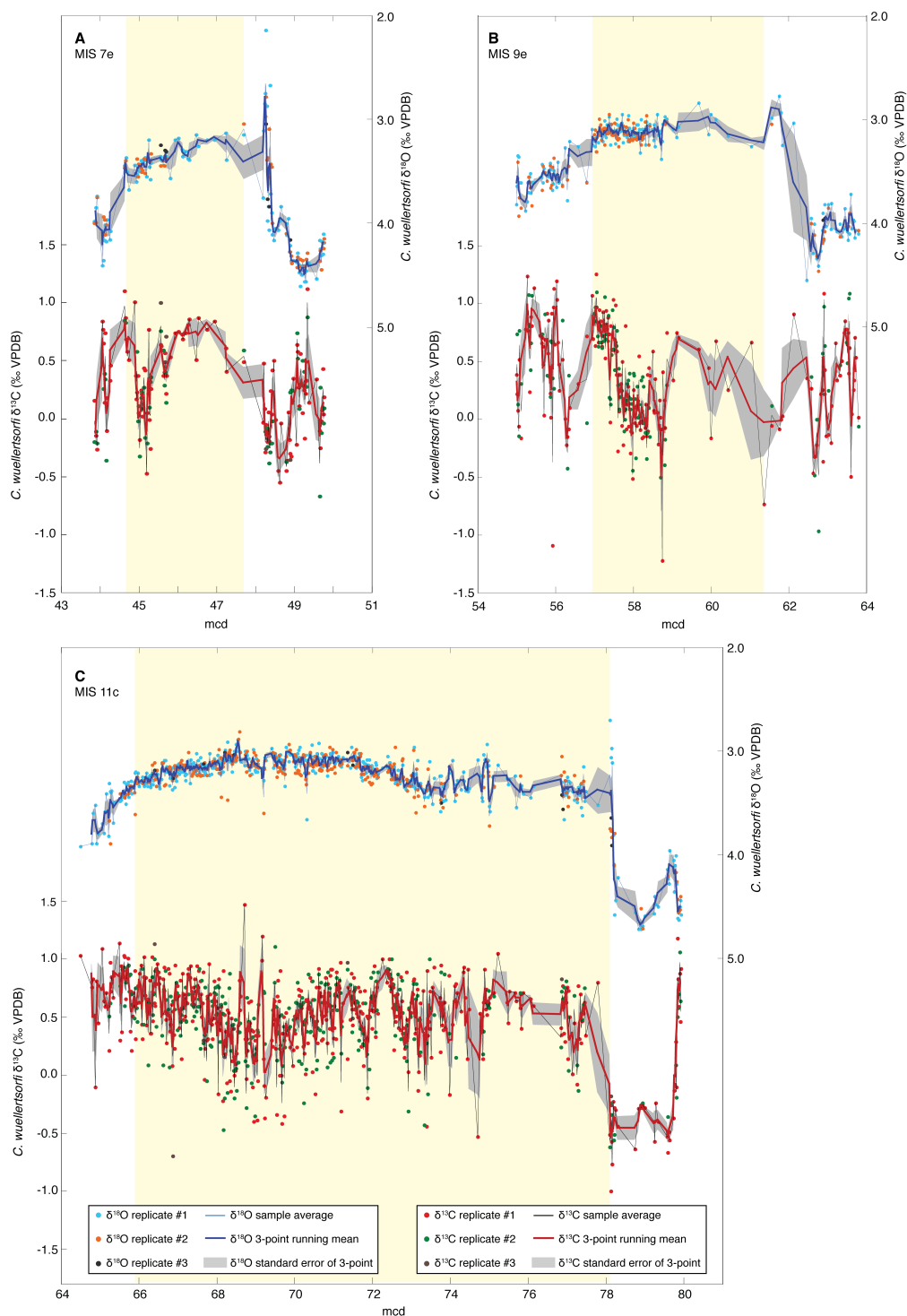
- 749 53. T. Fronval, E. Jansen, H. Hafliðason, H. P. Sejrup, Variability in surface and deep
750 water conditions in the nordic seas during the last interglacial period. *Quat. Sci. Rev.*
751 **17**, 963-985 (1998).
- 752 54. J. E. T. Channell *et al.*, *Expedition 303 Summary*. Proceeding of the Integrated Ocean
753 Drilling Program (Integrated Ocean Drilling Program Management International Inc.,
754 2006), vol. 303/306. doi:10.2204/iodp.proc.303306.101.2006
- 755 55. N. Irválı *et al.*, Rapid switches in subpolar North Atlantic hydrography and climate
756 during the Last Interglacial (MIS 5e). *Paleoceanography* **27**, PA2207 (2012).
- 757 56. C. Laj, X. Morin, the Shipboard Scientific Party, MD132-P.I.C.A.S.S.O/IMAGES XI
758 cruise report, Les rapports de campagne à la mer, No. *OCE/2004/02* (Plouzané, France,
759 2004).
- 760 57. K. E. Kohfeld, R. G. Fairbanks, S. L. Smith, I. D. Walsh, Neogloboquadrina
761 pachyderma (sinistral coiling) as paleoceanographic tracers in polar oceans: Evidence
762 from Northeast Water Polynya plankton tows, sediment traps, and surface sediments.
763 *Paleoceanography* **11**, 679-699 (1996).
764
765



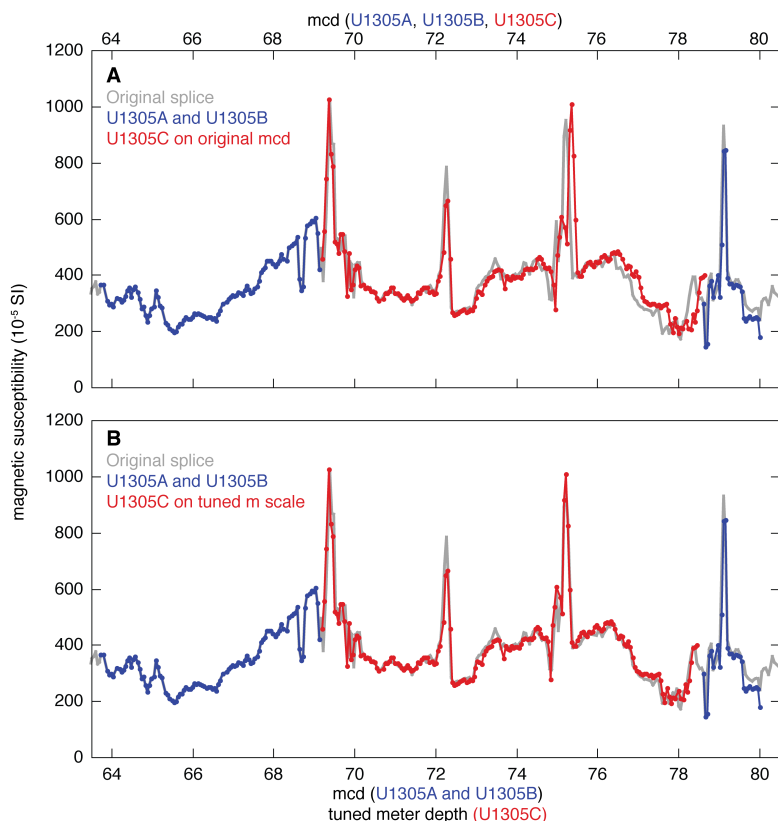
766

767 **Fig. S1. Eirik Drift *C. wuellerstorfi* (*sensu stricto*) replicate stable isotope values for**
 768 **different cleaning procedures.** Cross-plots comparing sample replicate measurements where
 769 sufficient *C. wuellerstorfi* tests were present to allow it (n=493): A) Site U1305 *C.*
 770 *wuellerstorfi* $\delta^{13}\text{C}$ values of tests visually cleaned using a brush and distilled water ('brush-
 771 cleaned'; sample average; x-axis) plotted versus tests cleaned using the standard protocol
 772 involving methanol (yellow circles), Site U1305 *C. wuellerstorfi* $\delta^{13}\text{C}$ values of brush-cleaned
 773 versus brush-cleaned tests (red circles), and MD03-2664 *C. wuellerstorfi* $\delta^{13}\text{C}$ values of
 774 standard-cleaned vs. standard-cleaned tests (blue circles; 10). B) Same as in A) but for *C.*
 775 *wuellerstorfi* $\delta^{18}\text{O}$. Note the similarity in stable isotope values for the different cleaning
 776 protocols. C) Umbilical (lef), apertural (middle), and spiral view (right) of an example
 777 specimen of *C. wuellerstorfi sensu stricto* from Site U1305 Hole C, 8H-3, 100-102 cm.

778
779
780
781
782
783
784
785
786
787
788
789
790
791
792
793
794
795
796

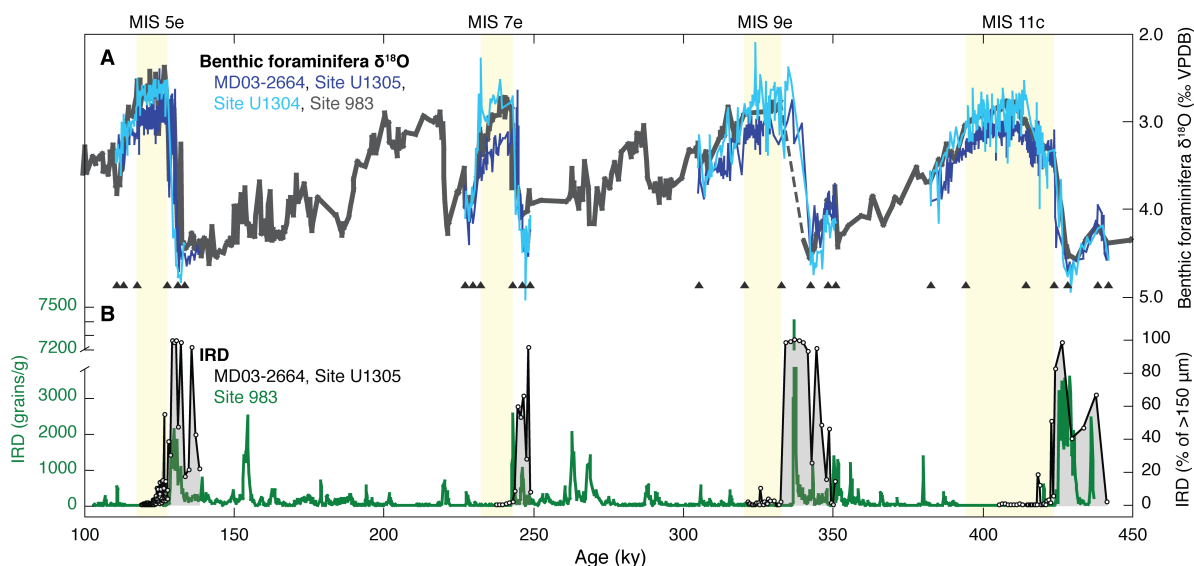


797
798 **Fig. S2. Stable isotope results.** The Site U1305 *C. wuellerstorfi* $\delta^{13}\text{C}$ (red) and $\delta^{18}\text{O}$ (blue)
799 records for A) MIS 7e, B) MIS 9e, and C) MIS 11c plotted versus core depth (meter composite
800 depth; mcd) showing all individual data points (dots; see inset at bottom for color coding), the
801 sample average values (thin lines), the three-point running mean (bold lines), and the standard
802 error of the mean of three-point running window (gray shading; includes on average five
803 individual data points).
804



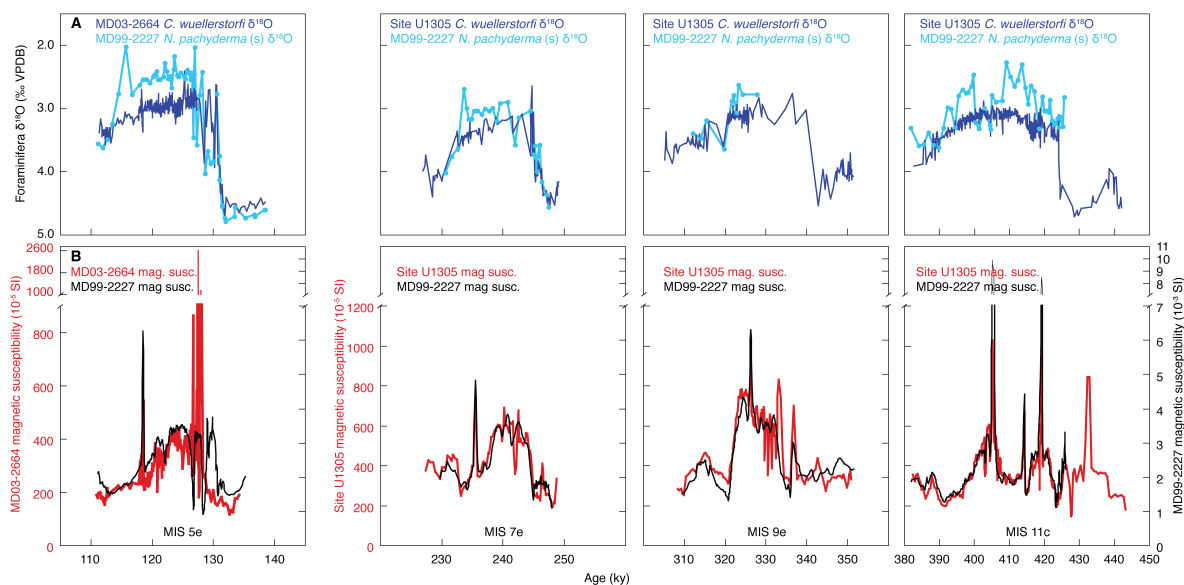
805
 806 **Fig. S3. Hole U1305C MIS 11c meter depth scale tuning.** A) Magnetic susceptibility (54) of
 807 the original splice (gray) and our sampled intervals of U1305A and U1305B (blue) and
 808 U1305C (red) on the original mcd scale. Note the offset between U1305C and the original
 809 splice over ~ 74.5 - 78.5 mcd. B) Magnetic susceptibility (54) of the original splice (gray)
 810 and our sampled intervals of U1305A and U1305B (blue) on mcd, and our sampled interval of
 811 U1305C (red) on the tuned meter depth scale.

812
 813
 814
 815
 816
 817
 818
 819
 820
 821
 822
 823
 824
 825
 826
 827
 828
 829



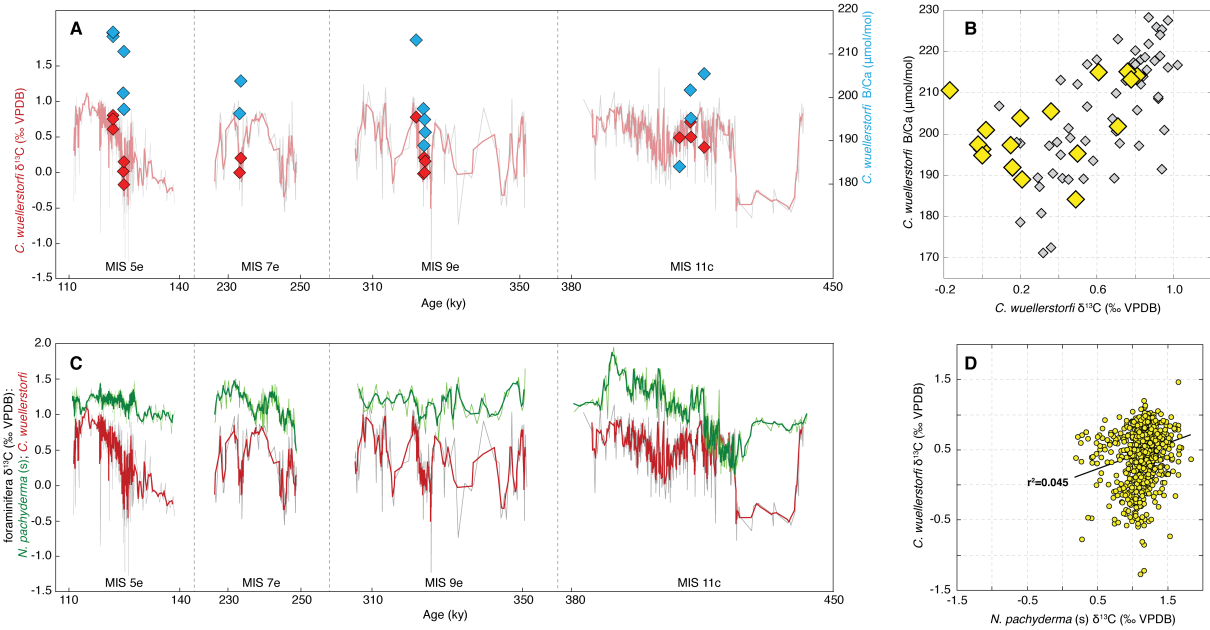
830
 831 **Fig. S4. Age model correlation.** Plotted on LR04 age (ky): A) Benthic foraminifera $\delta^{18}\text{O}$ from
 832 MD03-2664 (dark blue; MIS 5e) (10), Site U1305 (dark blue; MIS 7e, 9e, and 11c), Site
 833 U1304 (light blue) (15, 38), and age model correlation target Site 983 (gray) (33) with tie
 834 points denoted by triangles; B) Site 983 ice-rafted debris (IRD) as grains gram^{-1} (45) compared
 835 to NW Atlantic IRD (black with gray shading) from MD03-2664 (MIS 5e) (55) and Site
 836 U1305 as percent IRD grains in total entities $>150 \mu\text{m}$ shown only for the deglacial intervals
 837 where it was used to guide the age model construction. Dashed line in A) marks a prolonged
 838 interval lacking Site 983 $\delta^{18}\text{O}$ data across the MIS 10 to 9e transition. Yellow shading denotes
 839 the interglacial $\delta^{18}\text{O}$ plateaus as in the main text.

840
 841
 842
 843
 844
 845
 846
 847
 848
 849
 850
 851
 852
 853
 854
 855
 856
 857
 858
 859
 860
 861



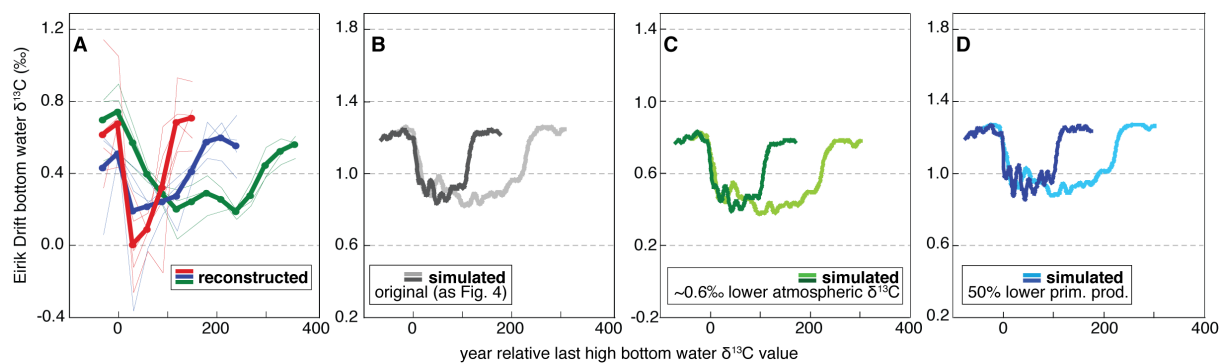
862
 863 **Fig. S5. Magnetic susceptibility correlation of MD03-2664/Site U1305 and MD99-2227.**
 864 Plotted on the LR04 age scale obtained from transferring our $\delta^{18}\text{O}$ -based age models of MD03-
 865 2664 (MIS 5e) and Site U1305 (MIS 7e, 9e, and 11c) to MD99-2227 by correlating magnetic
 866 susceptibility: A) epibenthic foraminifera *C. wuellerstorfi* $\delta^{18}\text{O}$ from core MD03-2664 (dark
 867 blue; MIS 5e) (10) and Site U1305 (dark blue; MIS 7e, 9e, and 11c) and planktic *N.*
 868 *pachyderma* (s) from core MD99-2227 (light blue) (32); B) magnetic susceptibility for MD03-
 869 2664 (red; MIS 5e) (56), Site U1305 (red; MIS 7e, 9e, and 11c) (54), and MD99-2227 (black)
 870 (47).

871
 872
 873
 874
 875
 876
 877
 878
 879
 880
 881
 882
 883
 884
 885
 886
 887
 888
 889
 890
 891
 892
 893



894
 895 **Fig. S6. Eirik Drift *C. wuellerstorfi* $\delta^{13}\text{C}$, *C. wuellerstorfi* B/Ca, and *N. pachyderma* (s)**
 896 **$\delta^{13}\text{C}$.** A) The Eirik Drift *C. wuellerstorfi* B/Ca values (blue diamonds) of tests combined from
 897 selected intervals in MIS 5e (core MD03-2664), 7e, 9e, and 11c (Site U1305), the average $\delta^{13}\text{C}$
 898 values of *C. wuellerstorfi* in the same intervals (red diamonds), and the full *C. wuellerstorfi*
 899 $\delta^{13}\text{C}$ time series shaded in the background for comparison (thin gray line, sample average; bold
 900 red line: 3-point running mean) over MIS 5e (MD03-2664; 10), 7e, 9e, and 11c (Site U1305)
 901 plotted versus age (ky; LR04). B) Cross-plot of the Eirik Drift *C. wuellerstorfi* $\delta^{13}\text{C}$ and B/Ca
 902 data (yellow diamonds; comparing the red and blue diamonds from A)) compared to the
 903 equivalent data of the last glacial-to-Holocene intervals of cores BOFS 5K (50°42'N,
 904 21°54'W; 3547 m w.d.; B/Ca from *C. wuellerstorfi* and *C. mundulus*; $\delta^{13}\text{C}$ from *Cibicidoides*
 905 spp.) and BOFS 8K (52°30'N, 22°06'W; 4045 m w.d.; B/Ca from *C. wuellerstorfi* and *C.*
 906 *mundulus*; $\delta^{13}\text{C}$ from *C. wuellerstorfi*) (gray diamonds; B/Ca data from Yu et al. (52), adjusted
 907 by +5% to correct for inter-laboratory differences; $\delta^{13}\text{C}$ data from Yu et al. (52) and references
 908 therein). C) The Eirik Drift *C. wuellerstorfi* $\delta^{13}\text{C}$ (coloring and references as in A)) and *N.*
 909 *pachyderma* (s) $\delta^{13}\text{C}$ from MIS 5e (MD03-2664; 55) and MIS 7e, 9e, and 11c (Site U1305; this
 910 study). The *N. pachyderma* (s) data were corrected by +1.0‰ to account for disequilibrium
 911 (57). D) Cross-plot of Eirik Drift *N. pachyderma* (s) $\delta^{13}\text{C}$ (also corrected by +1.0‰) versus *C.*
 912 *wuellerstorfi* $\delta^{13}\text{C}$ (sample average values; data and references as in C)) where the solid line
 913 shows the linear fit ($r^2=0.045$).

914
 915
 916
 917
 918
 919
 920
 921
 922
 923



924
 925 **Fig. S7. Reconstructed and simulated Eirik Drift bottom water $\delta^{13}\text{C}$ variability.** Plotted
 926 versus years relative the final high values preceding distinct bottom water $\delta^{13}\text{C}$ reductions at
 927 the Eirik Drift: A) reconstructed bottom water (*C. wuellerstorfi*) $\delta^{13}\text{C}$ changes shown as
 928 averages (bold lines) of individual events from MIS 1, 5e, 9e, and 11c (thin lines) at 30-year
 929 steps (obtained by linear interpolation) and binned according to durations of <100 (red; n=5),
 930 101-200 (blue; n=4), and 201-300 years (green; n=3); for the same two simulated NADW
 931 shoaling events (showing ten-year running means): B) the original simulation as shown in Fig.
 932 4; C) the original simulation but with atmospheric $\delta^{13}\text{C}$ decreased by $\sim 0.6\text{‰}$ and fixed (at -
 933 7.1‰); and D) the original simulation but with 50% decreased primary productivity in the
 934 northern deep water formation regions off southern Greenland and in the Nordic Seas.

935
 936

937 **Data S1. (separate file)**

938 Data S1_Eirik-Drift_MIS-7e-9e-11c.xlsx